



Cite as
Nano-Micro Lett.
(2025) 17:8

Received: 26 June 2024
Accepted: 16 August 2024
© The Author(s) 2024

Crystallization Modulation and Holistic Passivation Enables Efficient Two-Terminal Perovskite/CuIn(Ga)Se₂ Tandem Solar Cells

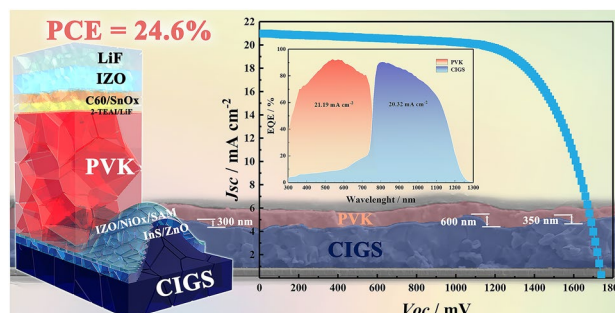
Cong Geng¹, Kuanxiang Zhang², Changhua Wang², Chung Hsien Wu², Jiwen Jiang², Fei Long³, Liyuan Han⁴ ✉, Qifeng Han⁴, Yi-Bing Cheng¹, Yong Peng¹ ✉

HIGHLIGHTS

- Integrating perovskite solar cells onto irregular rough CuIn(Ga)Se₂ (CIGS) surfaces remains a challenge; new strategy was explored to develop monolithic perovskite/CIGS tandem solar cell by manipulating the crystallization of perovskite.
- Surface reconstruction and field-effect passivation are developed synergistically to issue complex interface relationship between perovskite and C60.
- The champion power conversion efficiency (PCE) of 24.6% realized, providing significant commercial opportunities for all thin-film-based perovskite/CIGS tandem cells.

ABSTRACT Two-terminal (2-T) perovskite (PVK)/CuIn(Ga)Se₂ (CIGS) tandem solar cells (TSCs) have been considered as an ideal tandem cell because of their best bandgap matching regarding to Shockley–Queisser (S–Q) limits. However, the nature of the irregular rough morphology of commercial CIGS prevents people from improving tandem device performances. In this paper, D-homoserine lactone hydrochloride is proven to improve coverage of PVK materials on irregular rough CIGS surfaces and also passivate bulk defects by modulating the growth of PVK crystals. In addition, the minority carriers near the PVK/C60 interface and the incompletely passivated trap states caused interface recombination. A surface reconstruction with 2-thiopheneethylammonium iodide and *N,N*-dimethylformamide assisted passivates the defect sites located at the surface and grain boundaries. Meanwhile, LiF is used to create this field effect, repelling hole carriers away from the PVK and C60 interface and thus reducing recombination. As a result, a 2-T PVK/CIGS tandem yielded a power conversion efficiency of 24.6% (0.16 cm²), one of the highest results for 2-T PVK/CIGS TSCs to our knowledge. This validation underscores the potential of our methodology in achieving superior performance in PVK/CIGS tandem solar cells.

KEYWORDS PVK/CIGS TSCs; Irregular rough surfaces; Modulating the growth; PVK/C60 interface recombination



✉ Liyuan Han, han.liyuan@sjtu.edu.cn; Yong Peng, yongpeng@whut.edu.cn

¹ State Key Laboratory of Advanced Technology for Materials Synthesis and Processing, Wuhan University of Technology, Wuhan 430070, People's Republic of China

² Triumph Photovoltaic Materials Co., Ltd., No. 1001 Yannan Avenue, High-Tech Development District, Bengbu, Anhui 233000, People's Republic of China

³ College of Materials Science and Engineering, Guilin University of Technology, Guilin 541004, People's Republic of China

⁴ State Key Laboratory of Metal Matrix Composites, Shanghai Jiao Tong University, Shanghai 200240, People's Republic of China



1 Introduction

Two-terminal (2-T) perovskite (PVK)/CuIn(Ga)Se₂ (CIGS) tandem solar cells (TSCs) have been considered as one of the most promising tandem technologies because of their bandgap matching capacity, regarding to Shockley–Queisser (S-Q) limit [1–3]. However, this tandem technology has been suffering from low performances in past years [4–8].

An obstacle of fabricating high-performance PVK/CIGS TSCs is the nature of the irregular rough surface morphology of commercial CIGS, which is typical lateral feature sizes in the order of 500 nm to 1 μm randomly distributing on CIGS surface [2, 7]. Consequently, incomplete surface coverage and shunt paths can easily take place while fabricating tandem devices [2, 9]. A chemical mechanical polishing interconnection layer strategy was used by Han et al. to smoothen surfaces, while Jošt et al. chose a highly technological co-evaporation method to prepare a uniform active CIGS surface [10, 11]. However, no whether polishing the interconnection layer or modifying CIGS preparing technology to obtain a smooth surface is costly and incompatible with industry. It is necessary to manipulate the deposition of top-cells. Normally, the growth orientation of the PVK crystals on the substrate is not under control, particularly in the case of more complex rough surfaces, resulting in disordered growth of grain. Strategies can be explored to manipulate the crystallization of PVK, to achieve the preferred orientation of grain growth to fully cover irregular (nano) rough surfaces [12–16]. In addition, incomplete passivation of trap states in PVK films and minority carriers near the interface is prone to trigger interface recombination, in turn reducing the efficiency of the device [17–22]. Growing the non-uniform PVK absorbers on the rough surface of CIGS resulted in more defects, which require further enhanced quality and mitigated recombination losses [23–26].

In this work, D-homoserine lactone hydrochloride (D-HLH) was involved to modulate PVK crystal growth, passivate bulk defects, and also improve the contacts of PVK films on CIGS surfaces as a consequence. In this instance, D-HLH has the capacity to form hydrogen bonds [–O–C(=O)···H–N and –NH···I–] with FAI, as well as robust Pb–O bonds with PbI₂, which can control nucleation and crystal growth rates, and further improving crystal quality to cover irregular rough surfaces [27]. Furthermore, a surface reconstruction with 2-thiopheneethylammonium iodide (2-TEAI) and N,

N-dimethylformamide (DMF) assisted passivates the defect sites located at the PVK surface and grain boundaries [18]. Simultaneously, LiF is used to create this field-effect, repelling hole carriers away from the PVK and C60 interface and thus reducing recombination [28]. Through this synergistic strategy, a 2-T PVK/CIGS tandem achieved 24.6% (0.16 cm²) of power conversion efficiency (PCE), which is one of the highest results for 2-T PVK/CIGS solar cells in our knowledge. This validation demonstrates the potential of our approach to achieve high PCE-values in PVK/CIGS tandem solar cells.

2 Experimental Section

2.1 Materials

Lead iodide (PbI₂), lead bromide (PbBr₂), cesium iodide (CsI), formamidine hydroiodide (FAI), methylammonium bromide (MABr), 2-thiopheneethylammonium iodide (2-TEAI), C60 (99.99%) and bathocuproine (BCP) were purchased from Xi'an Yuri Solar Co., Ltd. Lithium fluoride (LiF) was purchased from Sigma-Aldrich. [2-(9H-carbazol-9-yl)ethyl]phosphonic acid (2PACz) was purchased from TCI. D-Homoserine lactone hydrochloride (D-HLH) and Anisole were purchased from Macklin. The IZO and NiO target were purchased from ZhongNuo Advanced Material (Beijing) Technology Co., Ltd. All the chemicals were used as received without further purification.

2.2 CIGS Solar Cells Fabrication

Triumph Photovoltaic Materials Co., Ltd., for providing products of commercial CIGS solar cells. CIGS is deposited via rapid-thermal processing; the substrate for the CIGS absorber (~1.5 μm) is a soda-lime glass on top of which a molybdenum (Mo) back contact is deposited via a direct-current (DC) magnetron sputtering. After the absorber deposition, the CIGS solar cells are completed with a 40–60 nm InS (Indium Sulfide) and a 60 nm i-ZnO (intrinsic zinc oxide).

2.3 Single-Junction Perovskite Solar Cells Fabrication

The ITO glass substrates underwent a sequential cleaning process, which involved sonication in detergent,

deionized water, and ethanol for durations of 15 min each. Substrates were subsequently dried using N_2 flow and exposed to ultraviolet-ozone treatment for a duration of 15 min. A self-assembled monolayers (SAM) of 2PACz (1 mg mL^{-1} in absolute ethanol) was spin-coated at 3000 rpm for 30 s on ITO and subsequently annealed at 100°C for 10 min in N_2 glovebox. Next, $1.4 \text{ M Cs}_{0.05}(\text{FA}_{0.83}\text{MA}_{0.17})_{0.95}\text{Pb}(\text{I}_{0.83}\text{Br}_{0.17})_3$ PVK precursor solution was prepared by dissolving a mixture of FAI, MABr, CsI, PbI_2 , and PbBr_2 in a mixed DMF:DMSO (4:1 v/v). D-HLH was added to the precursor solution at optimized concentrations (0.5 mg mL^{-1}). The PVK films were spin-coated at 2000 rpm for 45 s, then followed with 7000 rpm for 10 s. Anisole of 300 μL was dropped in the center of the substrates 12 s before the end of the spin-coating process. Subsequently, the substrates were immediately transferred onto a hotplate of 100°C and were annealed for 15 min. For the devices with surface passivation treatment, 2-TEAI (1 mg mL^{-1}) was dissolved in a mixed solvent of IPA:DMF (150:1, v/v), spun onto the as-prepared PVK films at 5,000 rpm for 30 s, and then annealed at 100°C for 5 min. After cooling to room temperature, the annealed films were washed by 100 μL IPA with the same spin coating procedure mentioned above, and then the washed film was transferred to a 100°C hot plate and dried for 3 min. Sequentially thermally deposited LiF (1 nm), C60 (25 nm), BCP (6 nm) and silver (100 nm) to complete the device.

2.4 PVK/CIGS Tandem Solar Cell Fabrication

The CIGS cell fabrication process for 2 T TSCs is followed as described before up to the $i\text{-ZnO}_x$ layer. After that, a 20 nm of indium-doped zinc oxide (IZO) is sputtered to serve as recombination layer. As hole transporting layer, nanocrystalline NiOx with a thickness of $\sim 15 \text{ nm}$ was sputtered from NiO target (99.9%) in an Ar atmosphere using Angstrom Engineering EvoVac system. The 2PACz, PVK, LiF and C60 (15 nm) layers are deposited in the same way as with the single-junction perovskite solar cells (PSCs). Instead of BCP, a 20 nm of SnO_2 was deposited by atomic layer deposition (ALD) in an Arradiance GEMStar reactor. A transparent front electrode (70 nm of IZO) is sputtered from a IZO ceramic target on top of the SnO_2

through a shadow mask to overlap of the Mo back electrode at 43 W. Ag finger with a thickness of 300 nm was thermally evaporated using shadow mask. Finally, 100 nm LiF was thermally evaporated as an anti-reflection layer.

2.5 Characterizations

The surface and cross-sectional morphology of the PVK films were acquired by scanning electron microscopy (SEM) (QUA TTROS, Thermal Fisher Scientific). ^1H NMR and ^{13}C NMR spectra were collected using a Bruker 400/600 MHz instrument Spectrometer. Fourier Transform Infrared Spectroscopy (FTIR) was performed by Thermo Scientific Nicolet iS20. X-ray photoelectron spectroscopy (XPS) measurement was carried out on a Thermo Scientific ESCALAB Xi + system with a monochromatized Al $K\alpha$ (for XPS mode) under a pressure of $5.0 \times 10^{-7} \text{ Pa}$. X-ray diffraction (XRD) data were obtained by using a Bruker D8 Advance diffractometer. The surface morphology of the PVK film was collected by atomic force microscope (AFM) (Park XE7). The PL spectra were obtained using a PL microscope (Flex One, Zolix, China). Time-resolved PL measurements were conducted using a Delta Flex Fluorescence Lifetime System (Horiba Scientific Com, Japan) under excitation at 470 nm light pulse. C-V curves were measured using an EC-lab (SP300) instrument. The J - V curves were measured under AM 1.5 G sunlight (100 mW cm^{-2}), using a solar simulator (Oriel 94023A, 300 W) and Keithley 2400 source meter. The J - V measurements were conducted with a scan rate of 100 mV s^{-1} (voltage step of 10 mV and delay time of 100 ms) from open voltage to short circuit in forward (-0.1 to 1.2 V) and reverse (1.2 to -0.1 V) directions at room temperature in the air. A mask with an aperture area of 0.16 cm^2 for tandem device was used. No preconditioning protocol, such as light soaking or forward voltage bias applied for a long time, was used before starting the measurement. The steady-state PCE was determined by the time series of power output at the maximum power point voltage extracted from the J - V curves. For the maximum power point stability testing, encapsulated devices were exposed to continuous illumination by a simulated AM 1.5G one-sun illumination in open ambient air. External quantum efficiency (EQE) spectra of devices were measured using a solar cell quantum-efficiency measurement system. Photoluminescence quantum yield (PLQY) was measured by Enli Tech, with a 405 nm laser light source.



3 Results and Discussion

3.1 Crystallization Modulation and Holistic Passivation

An irregular (nano) rough (variation of ≈ 550 nm) commercial CIGS cell surface remains a key challenge for integrating the PVK sub-cell onto the top, as shown in Fig. 1a. Several hurdles hinder the achievement of high-performance devices: uncovered surface of CIGS (Fig. 1b), shunt paths, and inefficient charge collection in films. A PVK composition of $\text{Cs}_{0.05}(\text{FA}_{0.83}\text{MA}_{0.17})_{0.95}\text{Pb}(\text{I}_{0.83}\text{Br}_{0.17})_3$ (~ 1.63 eV) was applied with an additive engineering strategy to obtain reasonable surface coverage of CIGS. As anticipated, cross-sectional scanning electron microscope (SEM) reveals that the surface of CIGS is entirely coated with PVK film (Fig. 1c), and the irregular crystals transformed into vertical-growth monolithic grains with compact and dense morphology, resulting in a reduction in surface roughness (Fig. S1). Meanwhile, the introduction of D-HLH into PVK precursors can passivate bulk defects. On this basis, we combined surface/interface dual passivation to address the issue of carrier recombination at complex PVK/C60 interface. An effective surface reconstruction with 2-TEAI and DMF-assisted, which passivates the defects sites on located at the PVK surface and grain boundaries. And LiF as interlayer can provide effective field-effect passivation between PVK and

C60 interface. We explored the impact of these efforts on the performance of single-junction PSCs. The device architecture consists of ITO/SAM/PVK/C60/BCP/Ag (Fig. 1d). The additive engineering enabled a device performance improvement compared with the control devices, from average PCEs of $\sim 17.9\%$ to $\sim 19.1\%$ (Figs. 1e and S2). In comparison with single surface or interface passivated devices, the highest average PCE ($> 21.8\%$) is achieved with 2-TEAI/LiF combination (Figs. 1e and S2).

3.2 Mechanism of Modulated PVK Films Crystal Growth

In comparison with the non-continuous contact of the control, better coverage of the PVK film on the CIGS surface was observed in the top-view SEM images after the incorporation of D-HLH into the precursor, as anticipated (Fig. 2a, b). Furthermore, the enhancement of film quality and coverage on the CIGS substrate is also verified by the increased PVK peak (14.0°) intensity of (100) plane and the decrease in intensity of the CIGS peak in the X-ray diffraction spectroscopy (XRD) pattern (Fig. 2c). The peak intensity ratios of (100)/(110) and (100)/(111) were subsequently calculated and recorded as 3.22 and 2.75 (control), as well as 3.91 and 3.16 (D-HLH). The addition of D-HLH resulted in an

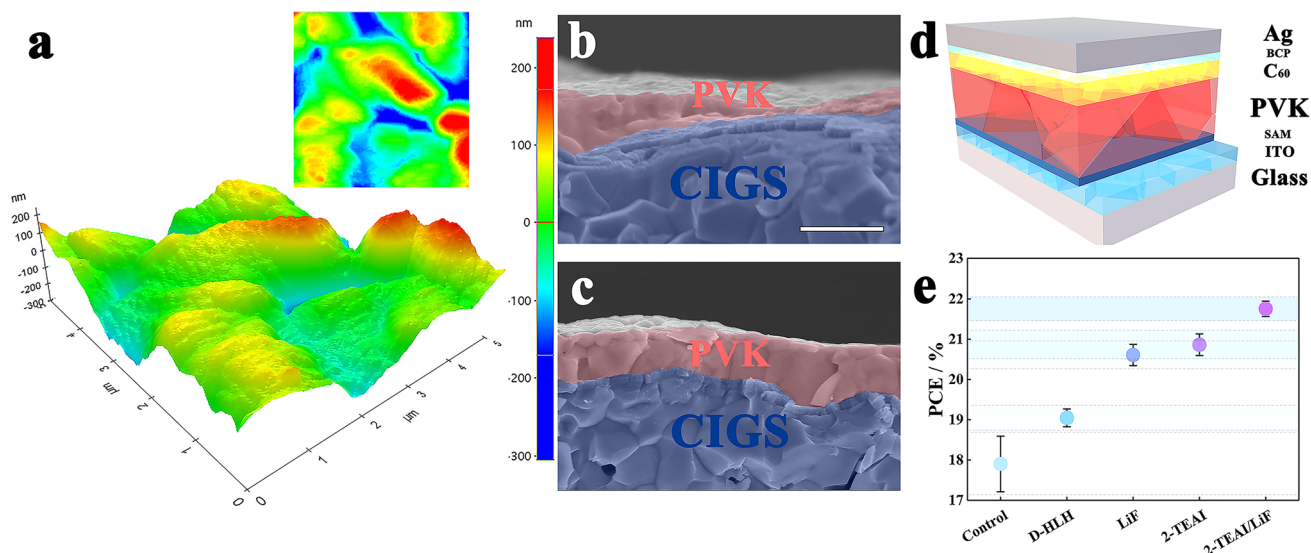


Fig. 1 Characteristics of the CIGS and p-i-n structured PSCs. **a** $5\ \mu\text{m} \times 5\ \mu\text{m}$ AFM topography of surface CIGS. Cross-sectional SEM images of PVK fabricated by **b** control and **c** additive engineering in PVK/CIGS tandem devices. (Scale bar: $1\ \mu\text{m}$) **d** Architecture of the single junction PSC device. **e** PCEs of control versus treated PSCs using different strategies

increase in the peak intensity ratio, suggesting a preferential orientation along the (100) direction. It is hypothesized that D-HLH can modulate the crystal growth of PVK, which aids achieve good crystallinity and coverage on rough surfaces.

Subsequently, we examined the impact of additives on the nucleation and crystallization process of PVK, a process that typically occurs swiftly during spin-coating and initial annealing. To ascertain this transformation process, XRD analysis was conducted (Fig. 2d). In the wet PVK film, complex intermediate phases such as $\text{MA}_2\text{Pb}_3\text{I}_8 \cdot 2\text{DMSO}$ ($2\theta = 6.73^\circ, 7.38^\circ, 9.33^\circ$) and $\delta\text{-FAPbI}_3$ ($2\theta = 11.9^\circ$) were formed in the control PVK due to the robust interaction between the PVK precursor and DMSO [13]. Upon the incorporation of D-HLH, the wet PVK films manifested amorphous characteristics without discernible crystallization, attributable to the hydrogen-bonding interaction between D-HLH and the PVK precursors. Subsequent to the application of the anti-solvent, a more pronounced peak intensity of $\alpha\text{-FAPbI}_3$ was observed compared to the control, suggesting that the film based on D-HLH demonstrates a higher nucleation rate relative to the control film. Consequently, dynamic light scattering (DLS) was employed to investigate the nucleation of the PVK precursor solution, as shown in Fig. 2e. The DLS peak center exhibited a shift from 65.55 to 91.01 nm in comparison with the control. The existence of larger colloids suggests that pre-nucleation has transpired in the PVK precursor solution introduced by D-HLH. This process lowers the energy barrier for nucleation during precipitation, thereby expediting the transition from an intermediate phase to preformed PVK nuclei. With annealing at 100 °C, the peak of α -phase rose and the width of the half-peak gradually narrowed. Moreover, as the annealing time progresses (0–30 s), the target film exhibits a relatively slower growth rate compared to the control film (Fig. S3). In conclusion, the D-HLH treatment inhibited the formation of a mixed intermediate phase by converting the diverse intermediate adducts into pure α -phase PVK nuclei during both nucleation and crystal growth stages. Meanwhile, higher nucleation rates and slower crystal growth with preferential orientation result in better film coverage on irregular rough CIGS surfaces. As illustrated in Fig. 2f, microcrystals grow rapidly in an oversaturated solution and stack randomly. This leads to the formation of discontinuous PVK films on the irregularly rough CIGS surface due to the random orientations of the growing PVK. In contrast, when the D-HLH additive is incorporated, optimal nucleation of

PVK is achieved, along with slower crystal growth and preferential orientation, thereby achieving higher quality and vertically oriented PVK films to fully cover the irregular rough surface of CIGS.

The liquid-state proton nuclear magnetic resonance (^1H NMR) measurement was conducted to investigate the chemical interaction between additives and PVK precursors. This interaction dictates the formation of intermediate phases, thereby significantly influencing the crystallization process. In a pure deuterated DMSO solution, the ^1H resonance signal at 8.82 ppm, which originated from protonated ammonium in neat FAI, was split into two peaks at 8.95 and 8.82 ppm in the D-HLH + FAI system. Concurrently, the single peak at 7.878 ppm was divided into multiple peaks, suggesting the occurrence of a hydrogen bonding interaction between D-HLH and FA^+ ions (Fig. 2g). To substantiate this interaction, the pure D-HLH and the mixed solution of D-HLH + FAI were characterized using ^{13}C NMR. As depicted in Fig. S4, the ^{13}C NMR spectrum at 173.768 ppm of the pure D-HLH corresponds to the ester group. This group also experiences a corresponding shift in the mixed solution of D-HLH + FAI, thereby reinforcing the interaction between FAI and D-HLH. In addition, when PbI_2 was incorporated into the D-HLH solution, the ^1H peak of $-\text{NH}_3^+$ at 9.03 ppm was shifted to 8.53 ppm, implying that there also was an interaction between PbI_2 and the D-HLH, a larger shift amplitude implies that D-HLH had a stronger interaction with PbI_2 as compared to FAI (Fig. 2g). At the same time, it is found that the ^{13}C NMR peak is shifted to 173.772 ppm after the introduction of PbI_2 , which originates from the interaction between polar ester $[-\text{O}-\text{C}(=\text{O})-]$ and uncoordinated Pb^{2+} (Fig. 2h). These results confirm that D-HLH can interact with the FAI and PbI_2 , which affect its reaction rate, eventually modulating the PVK crystallization. Additional evidence of the interaction was obtained through Fourier transform infrared spectroscopy (FTIR) and X-ray photoelectron spectroscopy (XPS). In the FTIR spectra (Fig. 2i), the peaks corresponding to N–H stretching and C=O stretching shifted to lower wavenumbers following the incorporation of D-HLH, indicating an interaction between the PVK and the D-HLH molecule. The chemical environment of various components within the PVK was also examined using XPS (Fig. S5). In the case of Pb^{2+} ions, the introduction of D-HLH led to a shift in the Pb 4f signal toward higher binding energies. This suggests that the ester group within D-HLH formed strong Pb–O bonds with the



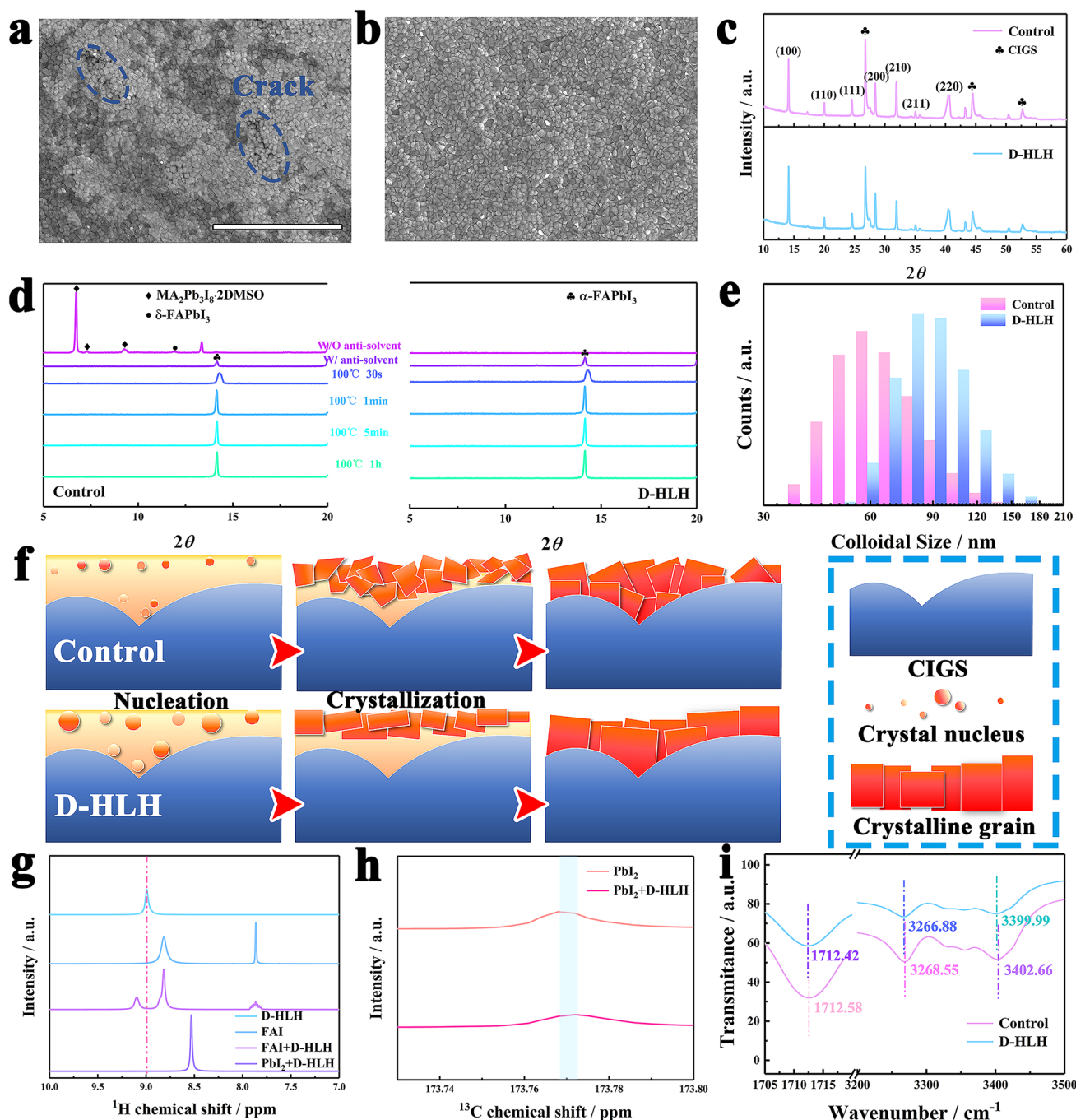


Fig. 2 Mechanism of the modulated crystal growth by additive. **a** Top-view SEM images of PVK of control and **b** D-HLH-treated as-grown on CIGS (Scale bar: 5 μm). **c** XRD patterns of the control and D-HLH-treated PVK films as-grown on CIGS. **d** Tracking of X-ray diffraction of the PVK films during three processes: wet PVK film without (w/o) anti-solvent during spin-coating, wet PVK film with (w) anti-solvent during spin coating, and PVK films annealed at 100 $^{\circ}\text{C}$ for various times. **e** DLS spectra of control and D-HLH incorporation into precursor solutions. **f** Schematic diagram of the crystal growth process of control and D-HLH-based precursor solutions on the surface of CIGS. **g** ^1H NMR spectra of D-HLH, FAI, FAI/D-HLH, and D-HLH/PbI₂. **h** ^{13}C NMR spectra of PbI₂ and PbI₂/D-HLH. **i** FTIR spectra of the control and D-HLH-treated PVK films

Pb^{2+} , resulting in a reduction in electron density on the Pb atoms. The observed shift in the I 3*d* peaks is attributed to the hydrogen bond ($-\text{N}-\text{H}\cdots\text{I}^-$) formed between the polar amino group of D-HLH and the electronegative iodide. Furthermore, the shift in the N 1*s* signal as evidenced by XPS indicates that D-HLH has the capacity to form hydrogen bonds with the amino groups in FA^+ . This interaction plays a crucial role in mitigating the loss of organic cations and reducing the density of defect states [29].

3.3 Effect Mechanism of the Surface/Interface Dual Passivation

The alterations in surface morphology resulting from various surface-treatment processes were validated using top-view SEM (Fig. 3a). The morphology of the PVK films remained almost unchanged for the 2-TEAI-treated, while after LiF evaporation, LiF clusters are formed on the surface of the PVK film. Meanwhile, the XRD patterns of PVK are nearly identical, and no clear two-dimensional (2D) PVK phase is observed (Fig. 3b). Surface-sensitive grazing-incidence wide angle X-ray scattering (GIWAXS) further revealed a peak at low scattering vectors $q \approx 0.6 \text{ \AA}^{-1}$ ($2\theta = 8.7^\circ$) in the 2-TEAI-based film, which corresponds to the 2-TEAI powder or film, indicating no low-dimensional PVK formed (Fig. 3c) [30]. Meanwhile, DMF-assisted reconstruct the PVK surface, providing more active A-site available for 2-TEA cations substitution can significantly enhance the PVK crystal quality and eliminate non-perovskite yellow phase $\delta\text{-CsPbI}_3$ ($q \approx 0.71 \text{ \AA}^{-1}$) at the surface [31].

^1H NMR spectra (Fig. 3d) also showed that the amino proton peak of FAI at 8.82 ppm was split into two broader peaks after mixing with 2-TEAI. These changes indicated stronger hydrogen bonding interactions between 2-TEAI and FA^+ ions. Due to such a strong interaction, 2-TEAI is likely to attach at the A sites in an ABX_3 PVK. We assessed surface passivation using XPS, as shown in Fig. 3e. XPS data of only LiF-coated PVK showed that the chemical environment of lead and iodine is not appreciably modified because fluoride ions did not form strong chemical bonds with lead. However, with dual surface/interface passivation, the Pb 4*f* peaks of the passivated PVK film shifted toward a lower binding energy of 0.21 eV compared with the D-HLH-based film, which could be due to ionic bond between 2-TEA⁺ and

PbI_6^{4-} , hydrogen bond of 2-TEA⁺ with I^- , and/or coordination between S and Pb^{2+} .

To demonstrate the effect of surface or interface treatment, we quantified the nonradiative recombination loss at the PVK/C60 interface using quasi-Fermi level splitting (QFLS). We measured the photoluminescence quantum yield (PLQY) of PVK films on glass/ITO/SAM with and without C60 deposition (Fig. S6). The corresponding QFLS values are 1179, 1200, 1205, 1218, and 1220 mV for control, D-HLH, LiF, 2-TEAI, and 2-TEAI/LiF samples, respectively (Fig. 3f). The significant changes in QFLS indicate the effectiveness of D-HLH and 2-TEAI in passivating bulk and surface PVK defects. However, the introduction of the C60 layer caused significant interfacial non-radiative recombination in the control stack. The LiF-induced field-effect effectively suppressed non-radiative recombination. The sequential combination of 2-TEAI/LiF further eliminated it, as confirmed by the improvement of QFLS.

We conducted further evaluations on the carrier recombination kinetics of PVK films. The steady-state PL spectra indicated that non-radiative recombination was significantly inhibited (Fig. S7). The 2-TEAI/LiF surface/interface dual passivation demonstrated a higher PL emission intensity compared to single surface or interface passivation. And the fitted PL lifetime by transient PL is increased from 67 (control) to 79 (D-HLH), 81 (LiF), 106 (2-TEAI) and 152 ns (2-TEAI + LiF), respectively, after the corresponding passivation (Fig. 3g). Treatment with LiF showed little improvement in lifetime, reflecting its limited suppression of defect-induced surface recombination. Conversely, the PVK film subjected to 2-TEAI treatment exhibited a marked enhancement in the decay curve, indicative of an extended carrier lifetime attributable to the diminishment of surface defects. This trend indicates that the surface passivation of 2-TEAI and field-effect passivation of LiF can achieve the best surface/interface passivation. The variation in interfacial charge transfer rate subsequent to surface or interface passivation is manifested in the transient PL lifetime of the PVK/C60 stacks (Fig. S8). The results indicated that the PL lifetime decreases from 23.6 (control) to 19 (D-HLH), 18.4 (LiF), 17 (2-TEAI) and finally to 15.9 ns (2-TEAI/LiF).

The enhancement of the built-in potential (V_{bi}) further corroborated effective charge separation and mitigated non-radiative recombination, thereby yielding a high output voltage. Utilizing the Mott–Schottky relationship, the capacitance–voltage (C - V) curve was meticulously measured to

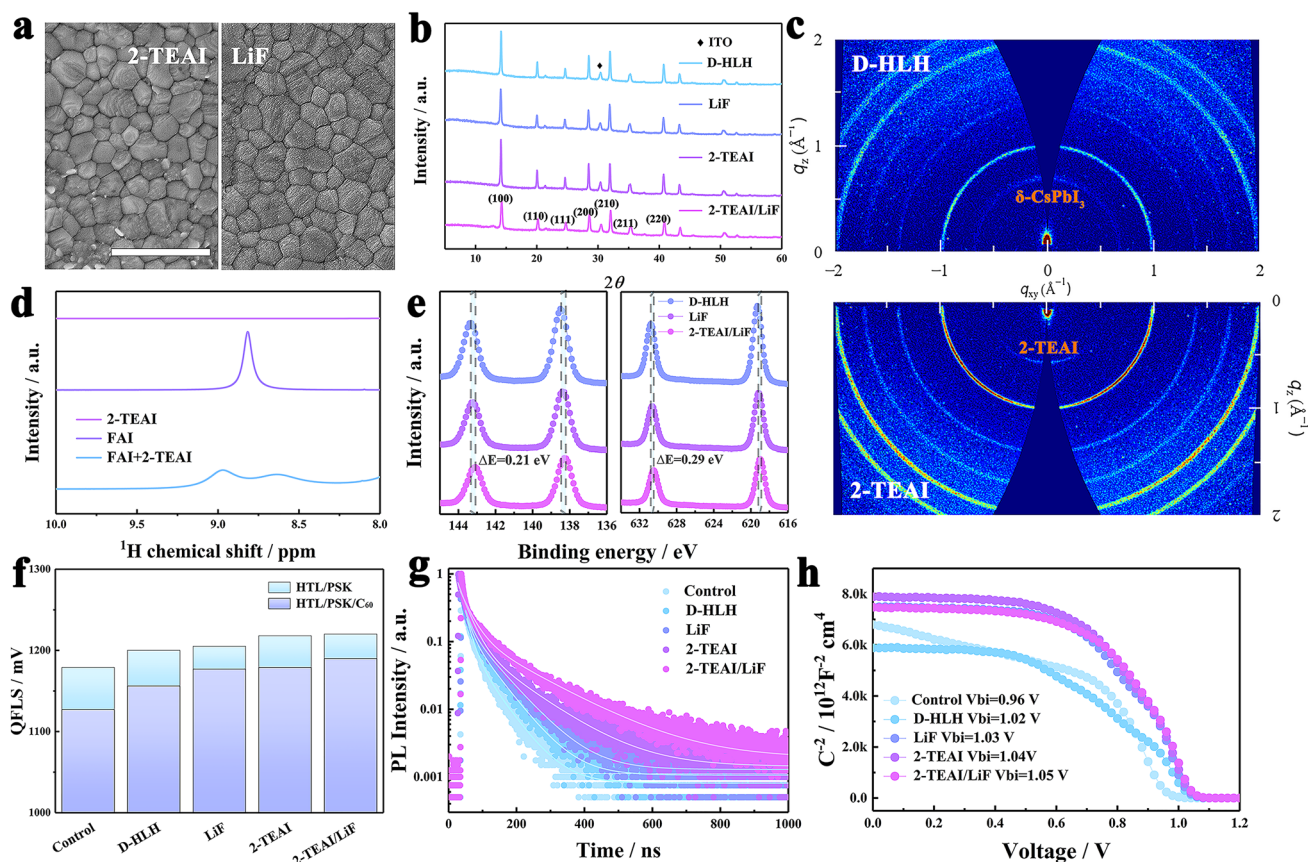


Fig. 3 Mechanism of surface/interface dual passivation. **a** Top-view SEM images of PVK surface with 2-TEAI and LiF-treated (Scale bar: 1 μm). **b** XRD pattern of PVK films. **c** GIWAXS patterns of the D-HLH-based and 2-TEAI-treated PVK films. **d** ^1H NMR spectra of 2-TEAI, FAI, and FAI with 2-TEAI. **e** High-resolution Pb 4*f* and I 3*d* XPS peaks of the PVK films. **f** Quasi-Fermi level splitting (QFLS) of films deposited on glass/ITO/SAM without and with C60. **g** Transient PL spectra for the glass/PVK samples. **h** Mott–Schottky plots for the corresponding devices

scrutinize the V_{bi} of the PVK film. As shown in Fig. 3h, the V_{bi} value of different devices increased from 0.96 (control) to 1.02 (D-HLH), 1.03 (LiF), 1.04 (2-TEAI) and 1.05 V (2-TEAI+LiF).

3.4 2-T PVK/CIGS Tandem Solar Cells

Inspired by the enhanced performance of single-junction PSCs, we developed 2-T PVK/CIGS tandem solar cells with the aim of enhancing efficiency and pushing the boundaries of the future photovoltaic market. Figure 4a illustrates a schematic of the tandem configuration stack, and the structure of tandem device is Glass/Mo/CIGS/InS/i-ZnO/IZO/NiO_x/SAM/1.63 eV PVK/LiF/C60/ALD SnO₂/IZO/Ag. Here, a 20 nm indium zinc oxide (IZO) layer acted as the recombination junction, while the 15-nm-thick sputtered

NiO_x layer between the IZO-SAM interface effectively reduced shunting, and the full layer stack and layout for our 2 T PVK/CIGS TSCs are depicted in Fig. S9. Cross-sectional SEM images of tandem solar cells are shown in Figs. 4b and S10. Figure 4c presents the current density–voltage (J – V) curves of the best-performing different treated PVK/CIGS tandems; the corresponding photo-voltaic parameters are summarized in Figs. S11 and S12. The champion PVK/CIGS tandem device achieved a remarkable reverse-scan PCE of up to 24.6%, with a short-circuit current density (J_{SC}) of 20.97 mA cm^{-2} , open-circuit voltage (V_{OC}) of 1.742 V, and fill factor (FF) of 67.3%, whereas the control device showed the highest PCE of 20.9%, with a J_{SC} of 20.84 mA cm^{-2} , V_{OC} of 1.640 V, and FF of 61.2%, (Fig. 4d). And external quantum efficiency (EQE) spectra (Fig. 4e) exhibited a matching current density of 21.19 and

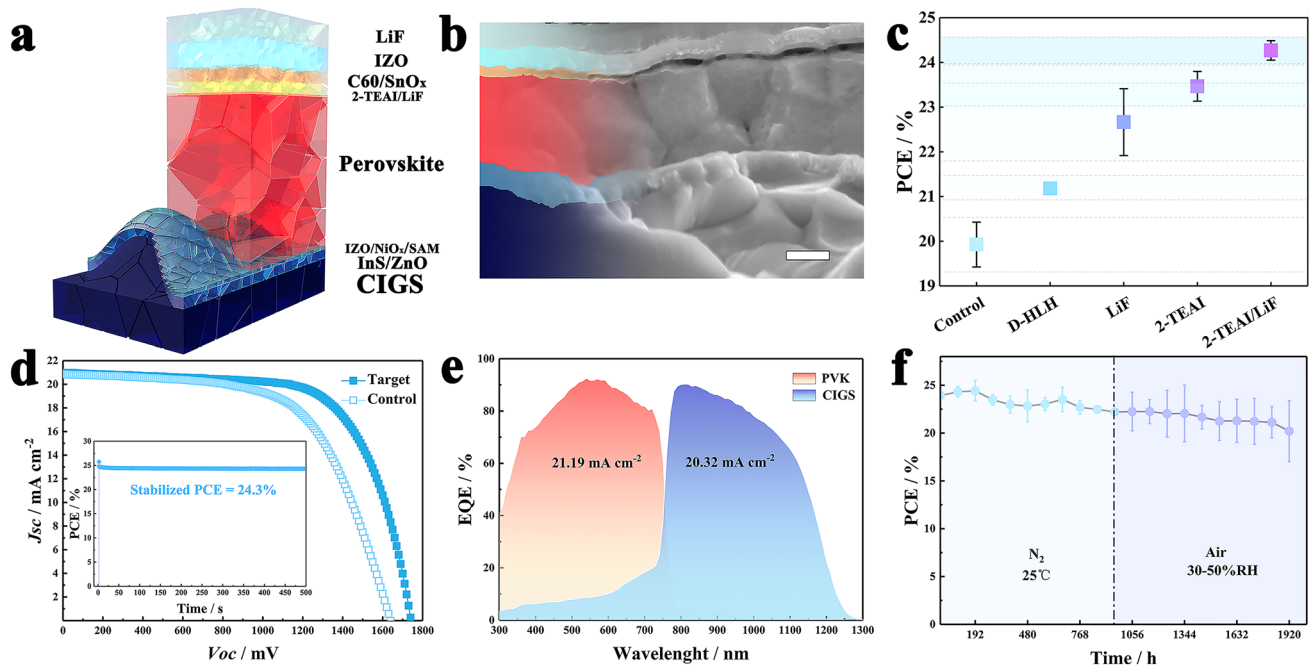


Fig. 4 Performance of the PVK/CIGS tandem solar cell. **a** Schematic structure of the 2-T PVK/CIGS tandem device. **b** Cross-sectional SEM image of the tandem device (Scale bar: 200 nm). **c** PCEs of control versus treated tandem devices using different strategies. **d** *J*-*V* characteristics of the best-performing tandem device with control and target. The inset shows the stabilized PCE of the champion device under maximum power point tracking. **e** EQE curves of PVK and CIGS sub-cells within the tandem device. **f** Stability of unencapsulated tandem devices in nitrogen to air

20.32 mA cm⁻² in PVK and CIGS sub-cells, respectively. The steady power output of champion tandem devices (*V*_{max} = 1.36 V) reached 24.3% after continuous illumination at 1 sun-simulated light for 500 s (Fig. 4d). Our tandem device is commensurate with the state-of-the-art 2-T PVK/CIGS tandem devices in literature (Table S1). In the study of the stability of unencapsulated tandem devices, *J*-*V* is regularly measured (Figs. 4f and S13). After 960 h of nitrogen storage, the cells maintained 92.8% of their initial efficiency. Subsequently, after being exposed to an air environment with a humidity level of 30%–50% for the same period, its efficiency remained at 84.4% of the initial efficiency.

4 Conclusions

Controlling the crystal growth of PVK to cover the rough surface of CIGS, while further improving crystal quality. Surface reconstruction passivates the defects sites located at the surface and grain boundaries. Meanwhile, creating a field-effect that repels hole carriers outside the interface between PVK and C60 reduces recombination. Realizing both bulk and surface/interface passivation by the combined

use of D-HLH, 2-TEAI, and LiF has mitigated PVK crystallization and complex interface carrier recombination issues. Through this synergistic strategy, a 2-T PVK/CIGS tandem achieved 24.6% (0.16 cm²) of PCE. The amalgamation of various functional regulation techniques presents a promising avenue for investigating the performance and stability of PVK-based tandems.

Acknowledgements The authors would like to thank Triumph Photovoltaic Materials Co., Ltd., for providing products of commercial CIGS solar cells. This work was supported by “National Natural Science Foundation of China (U21A20171, U20A20245),” “Hubei Provincial Natural Science Foundation of China (2023AFA010),” “Independent Innovation Projects of the Hubei Longzhong Laboratory (2022ZZ-09)” and “Social Public Welfare and Basic Research Special Project of Zhongshan (2020B2015).”

Authors’ Contributions Cong Geng contributed to investigation, figure design, data curation, original draft writing, and conceptualization. Kuanxiang Zhang, Chung Hsien Wu and Changhua Wang contributed to data curation and conceptualization. Jiwen Jiang contributed to conceptualization. Fei Long contributed to conceptualization. Liyuan Han contributed to conceptualization, validation, review and editing, and supervision. Qifeng Han and Yi-Bing Cheng contributed to conceptualization, review and editing. Yong

Peng contributed to figure design, validation, conceptualization, review and editing, and supervision.

Declarations

Conflict of interest The authors declare no interest conflict. They have no known competing financial interests or personal relationships that could have appeared to influence the work reported in this paper. Liyuan Han is an editorial board member for Nano-Micro Letters and was not involved in the editorial review or the decision to publish this article. All authors declare that there are no competing interests.

Open Access This article is licensed under a Creative Commons Attribution 4.0 International License, which permits use, sharing, adaptation, distribution and reproduction in any medium or format, as long as you give appropriate credit to the original author(s) and the source, provide a link to the Creative Commons licence, and indicate if changes were made. The images or other third party material in this article are included in the article's Creative Commons licence, unless indicated otherwise in a credit line to the material. If material is not included in the article's Creative Commons licence and your intended use is not permitted by statutory regulation or exceeds the permitted use, you will need to obtain permission directly from the copyright holder. To view a copy of this licence, visit <http://creativecommons.org/licenses/by/4.0/>.

Supplementary Information The online version contains supplementary material available at <https://doi.org/10.1007/s40820-024-01514-1>.

References

- H. Li, W. Zhang, Perovskite tandem solar cells: from fundamentals to commercial deployment. *Chem. Rev.* **120**, 9835–9950 (2020). <https://doi.org/10.1021/acs.chemrev.9b00780>
- M. Jošt, L. Kegelmann, L. Korte, S. Albrecht, Monolithic perovskite tandem solar cells: a review of the present status and advanced characterization methods toward 30% efficiency. *Adv. Energy Mater.* **10**, 1904102 (2020). <https://doi.org/10.1002/aenm.201904102>
- E. Alvianto, G. Wan, Z. Shi, H. Liang, X. Wang et al., Sustainable manufacturing of perovskite-CIGS tandem solar cells through lamination with metal-free transparent conductive adhesives. *ACS Energy Lett.* **9**, 2057–2064 (2024). <https://doi.org/10.1021/acsenenergylett.4c00350>
- Y. Xiong, Z. Yi, W. Zhang, Y. Huang, Z. Zhang et al., Recent advances in perovskite/Cu(In, Ga)Se₂ tandem solar cells. *Mater. Today Electron.* **7**, 100086 (2024). <https://doi.org/10.1016/j.mtelec.2023.100086>
- T. Todorov, T. Gershon, O. Gunawan, Y.S. Lee, C. Sturdevant et al., Monolithic perovskite-CIGS tandem solar cells via *in situ* band gap engineering. *Adv. Energy Mater.* **5**, 1500799 (2015). <https://doi.org/10.1002/aenm.201500799>
- Y.H. Jang, J.M. Lee, J.W. Seo, I. Kim, D.-K. Lee, Monolithic tandem solar cells comprising electrodeposited CuInSe₂ and perovskite solar cells with a nanoparticulate ZnO buffer layer. *J. Mater. Chem. A* **5**, 19439–19446 (2017). <https://doi.org/10.1039/c7ta06163c>
- M. Jošt, T. Bertram, D. Koushik, J.A. Marquez, M.A. Verheijen et al., 21.6%-efficient monolithic perovskite/Cu(In, Ga)Se₂ tandem solar cells with thin conformal hole transport layers for integration on rough bottom cell surfaces. *ACS Energy Lett.* **4**, 583–590 (2019). <https://doi.org/10.1021/acsenenergylett.9b00135>
- L. Zeng, L. Tang, Z. Luo, J. Gong, J. Li et al., A review of perovskite/copper indium Gallium selenide tandem solar cells. *Sol. RRL*, 2301059 (2024). <https://doi.org/10.1002/solr.202301059>
- Y. Hou, E. Aydin, M. De Bastiani, C. Xiao, F.H. Isikgor et al., Efficient tandem solar cells with solution-processed perovskite on textured crystalline silicon. *Science* **367**, 1135–1140 (2020). <https://doi.org/10.1126/science.aaz3691>
- M. Jošt, E. Köhnen, A. Al-Ashouri, T. Bertram, Š Tomšič et al., Perovskite/CIGS tandem solar cells: from certified 24.2% toward 30% and beyond. *ACS Energy Lett.* **7**, 1298–1307 (2022). <https://doi.org/10.1021/acsenenergylett.2c00274>
- Q. Han, Y.-T. Hsieh, L. Meng, J.-L. Wu, P. Sun et al., High-performance perovskite/Cu(In, Ga)Se₂ monolithic tandem solar cells. *Science* **361**, 904–908 (2018). <https://doi.org/10.1126/science.aat5055>
- C. Duan, J. Zhong, S. Hu, Y. Dou, J. Lu et al., Oriented growth for efficient and scalable perovskite solar cells by vapor–solid reaction. *Adv. Funct. Mater.* **34**, 2313435 (2024). <https://doi.org/10.1002/adfm.202313435>
- M. Li, R. Sun, J. Chang, J. Dong, Q. Tian et al., Orientated crystallization of FA-based perovskite via hydrogen-bonded polymer network for efficient and stable solar cells. *Nat. Commun.* **14**, 573 (2023). <https://doi.org/10.1038/s41467-023-36224-6>
- C. Zhang, H. Li, C. Gong, Q. Zhuang, J. Chen et al., Crystallization manipulation and holistic defect passivation toward stable and efficient inverted perovskite solar cells. *Energy Environ. Sci.* **16**, 3825–3836 (2023). <https://doi.org/10.1039/D3EE00413A>
- H. Gao, K. Xiao, R. Lin, S. Zhao, W. Wang et al., Homogeneous crystallization and buried interface passivation for perovskite tandem solar modules. *Science* **383**, 855–859 (2024). <https://doi.org/10.1126/science.adj6088>
- X. Jiang, B. Liu, X. Wu, S. Zhang, D. Zhang et al., Top-down induced crystallization orientation toward highly efficient p-i-n perovskite solar cells. *Adv. Mater.* **36**, e2313524 (2024). <https://doi.org/10.1002/adma.202313524>
- F. Ye, S. Zhang, J. Warby, J. Wu, E. Gutierrez-Partida et al., Overcoming C₆₀-induced interfacial recombination in inverted perovskite solar cells by electron-transporting carborane. *Nat. Commun.* **13**, 7454 (2022). <https://doi.org/10.1038/s41467-022-34203-x>
- X. Li, Z. Ying, J. Zheng, X. Wang, Y. Chen et al., Surface reconstruction for efficient and stable monolithic perovskite/silicon tandem solar cells with greatly suppressed residual strain. *Adv. Mater.* **35**, e2211962 (2023). <https://doi.org/10.1002/adma.202211962>
- R. Chen, J. Wang, Z. Liu, F. Ren, S. Liu et al., Reduction of bulk and surface defects in inverted methylammonium- and bromide-free formamidinium perovskite solar cells. *Nat. Energy* **8**, 839–849 (2023). <https://doi.org/10.1038/s41560-023-01288-7>

20. H. Chen, S. Teale, B. Chen, Y. Hou, L. Grater et al., Quantum-size-tuned heterostructures enable efficient and stable inverted perovskite solar cells. *Nat. Photon.* **16**, 352–358 (2022). <https://doi.org/10.1038/s41566-022-00985-1>
21. C. Liu, Y. Yang, H. Chen, J. Xu, A. Liu et al., Bimolecularly passivated interface enables efficient and stable inverted perovskite solar cells. *Science* **382**, 810–815 (2023). <https://doi.org/10.1126/science.adk1633>
22. Z. Liu, H. Li, Z. Chu, R. Xia, J. Wen et al., Reducing perovskite/C₆₀ interface losses via sequential interface engineering for efficient perovskite/silicon tandem solar cell. *Adv. Mater.* **36**, e2308370 (2024). <https://doi.org/10.1002/adma.202308370>
23. H. Liang, J. Feng, C.D. Rodríguez-Gallegos, M. Krause, X. Wang et al., 29.9%-efficient, commercially viable perovskite/CuInSe₂ thin-film tandem solar cells. *Joule* **7**, 2859–2872 (2023). <https://doi.org/10.1016/j.joule.2023.10.007>
24. X. Liu, J. Zhang, L. Tang, J. Gong, W. Li et al., Over 28% efficiency perovskite/Cu(InGa)Se₂ tandem solar cells: highly efficient sub-cells and their bandgap matching. *Energy Environ. Sci.* **16**, 5029–5042 (2023). <https://doi.org/10.1039/D3EE00869J>
25. J. Liu, M. De Bastiani, E. Aydin, G.T. Harrison, Y. Gao et al., Efficient and stable perovskite-silicon tandem solar cells through contact displacement by MgF₂. *Science* **377**, 302–306 (2022). <https://doi.org/10.1126/science.abn8910>
26. J. Liu, E. Aydin, J. Yin, M. De Bastiani, F.H. Isikgor et al., 28.2%-efficient, outdoor-stable perovskite/silicon tandem solar cell. *Joule* **5**, 3169–3186 (2021). <https://doi.org/10.1016/j.joule.2021.11.003>
27. Z. Zhang, J. Liang, J. Wang, Y. Zheng, X. Wu et al., Resolving mixed intermediate phases in methylammonium-free Sn-Pb alloyed perovskites for high-performance solar cells. *Nano-Micro Lett.* **14**, 165 (2022). <https://doi.org/10.1007/s40820-022-00918-1>
28. D. Menzel, A. Al-Ashouri, A. Tejada, I. Levine, J.A. Guerra et al., Field effect passivation in perovskite solar cells by a LiF interlayer. *Adv. Energy Mater.* **12**, 2201109 (2022). <https://doi.org/10.1002/aenm.202201109>
29. Z. Kang, Y. Tong, K. Wang, Y. Chen, P. Yan et al., Tailoring low-dimensional phases for improved performance of 2D–3D tin perovskite solar cells. *ACS Mater. Lett.* **6**, 1–9 (2024). <https://doi.org/10.1021/acsmaterialslett.3c00929>
30. Y. Du, D. Zhu, Q. Cai, S. Yuan, G. Shen et al., Spacer engineering of thiophene-based two-dimensional/three-dimensional hybrid perovskites for stable and efficient solar cells. *J. Phys. Chem. C* **126**, 3351–3358 (2022). <https://doi.org/10.1021/acs.jpcc.1c10210>
31. S.G. Ji, I.J. Park, H. Chang, J.H. Park, G.P. Hong et al., Stable pure-iodide wide-band-gap perovskites for efficient Si tandem cells via kinetically controlled phase evolution. *Joule* **6**, 2390–2405 (2022). <https://doi.org/10.1016/j.joule.2022.08.006>

Publisher's Note Springer Nature remains neutral with regard to jurisdictional claims in published maps and institutional affiliations.

